An Enhancement of LS-DYNA® XFEM Shells for Dynamic Ductile Failure Analysis

Y. Guo[1*], C. T. Wu[1], W. Hu[1], K. Takada[2], H. Okada[2], N. Ma[3], K. Saito[4]

[1]*Livermore Software Technology Corporation (LSTC), Livermore, CA 94551, USA*
[2]*Automobile R&D Center, Honda R&D Co., Ltd, Tochigi, 321-3393 Japan*
[3]*Center of Computational Welding Science (CCWS), Osaka University, Osaka, 567-0047 Japan*
[4]*Engineering Technology Division, JSOL Corporation, Tokyo, 104-0053, Japan*

Abstract

This paper presents an enhancement of LS-DYNA XFEM shell method [30] for dynamic ductile failure in shell structures. The XFEM shell formulation adopts the finite element continuous-discontinuous approach. The continuum damage model based on continuous displacements is used in the continuous stage to describe the diffuse micro-cracking in ductile failure before a macro-crack is formed. In the context of first-order shear deformable shell finite element method, a nonlocal modelling procedure based on a projection of mid-plane reference surface is introduced to regularize the element-wise strain fields induced by the continuum damage model. In the discontinuous stage, an incorporation of velocity discontinuities in shell finite elements is pursued by XFEM method when the damage variable exceeds a critical value and the transition from a continuous to a discontinuous model is permitted. A phantom-node approach [17] is employed in XFEM method to simplify the numerical treatment of velocity discontinuities in the shell finite element formulation. Several numerical benchmarks are examined using the explicit dynamics analysis and the results are compared with the experimental data to demonstrate the effectiveness and accuracy of the numerical method.

1. Introduction

Failure and fracture analyses in metal materials are increasingly important in many industries. For the automotive industry, lightweight materials such as the high-strength steel have a direct impact on driving dynamics, fuel consumption and agility. While the structure made of high-strength steel offers superior stiffness with reduced weight, material failure analysis in high-strength steel structure becomes critical for crashworthiness simulation in modern lightweight vehicle design. In contrast to brittle fracture in concretes and rocks, the ductile failure in metals undergoes a certain amount of plastic deformation before a macro-crack is evident. Microscopically, this ductile damage phenomenon is associated with voids nucleation, growth and coalescence under high and moderate stress triaxiality [1]. Macroscopically, the ductile damage is represented by the progressive degradation of material as a consequence of the growth of microstructural defects and can be modeled phenomenologically using the continuum damage mechanics [2,3]. When the coalescence of some microstructural defects creates the macro-crack, the discrete fracture becomes dominant as the ultimate result of the material degradation process [3] in ductile fracture.

Standard numerical simulations using the continuum damage models are known to be susceptible to the pathological localization of deformation. To regularize the non-unique solution in damage-induced strain localization problems, several integral-type and gradient-type of nonlocal damage models [4-6] and phase field model [7] based on regularized variational formulation were developed.

When the coalescence of some microstructural defects creates the macro-crack, the discrete fracture becomes dominant and rupture occurs in ductile materials. Unfortunately, the numerical methods based on a pure nonlocal damage model are inadequate to describe such kinematic discontinuity of the displacement field in a continuous setting [8]. To release the excessive straining in the damage zone and achieve a better representation of the entire failure process, many combined continuous-discontinuous approaches [8,9,10-13] have been developed. While the nonlocal damage model is used to describe the material degradation, the discontinuous

enrichment [14-16] typically used in fracture mechanics are usually considered to model the discrete crack. Among those discontinuous enrichment methods, the phantom-node approach [17] in extended finite element method (XFEM) [18, 19] is attractive to model the ductile fracture in plate and shell structures. The phantom-node approach describes a crack with two standard overlapping elements, therefore, it can be directly applied to any existing finite element code, for example, the 4-noded element using a fully integrated shear deformable shell formulation [21, 22].

In this study, we present a finite element continuous-discontinuous approach, which adopts nonlocal strain regularization in continuous damage models and phantom-node XFEM for discrete cracks, for the dynamic analysis of ductile failure in shell structures made of metals or alloys. The rest of the paper is organized as follows: Section 2 briefly summaries the XFEM shell formulations in LS-DYNA and provides the computational flow and keyword format to use XFEM. Section 3 describes a nonlocal approach for the XFEM method in shells for ductile fracture simulation. Three numerical examples are given in Section 4, and finally the conclusions are made in Section 5.

2. LS-DYNA XFEM Shell Formulations

The XFEM phantom-node approach has been applied to two finite element shell formulations in LS-DYNA, the one-point integrated Belytschko-Lin-Tsay shell with hourglass control [23] and the four-node fully integrated shear deformable shell formulation [21, 22] with assumed strain interpolants [24, 25] for alleviating the shear locking and for enhancing the in-plane bending behavior. Through-the-thickness, element-wise discontinuous velocity and angular velocity fields are introduced to the standard shell element formulation using the XFEM phantom-node approach to model the internal discontinuity in a shell element when fracture occurs in this element.

Unlike the brittle fracture where material failure is controlled by stress-based criterion, such as the maximum tensile strength in Mode-I fracture, the ductile failure is determined by strain-based criterion. With a standard plastic constitutive model, the transition from continuous to discontinuous state can be triggered when a critical plastic strain threshold is reached. In this case, a modified cohesive zone model is applied to the newly activated crack surface to account for the energy released from the crack surface. With the continuum damage model, the transition from damage to crack is triggered when the material is fully degraded. In this scenario, a traction-free crack [15,20] is introduced to the numerical model as the damage variable is close to one. These local material models cannot be directly used for numerical simulations of ductile fracture, nonlocal processing procedure needs to be applied to remove the mesh sensitivity problem, which will be presented in next section. Detailed theories on these element formulations and phantom-node XFEM can be found in relevant literatures and are omitted in this paper.

2.1 Computational flow chart

The computational procedure of the phantom-node XFEM is given in the following.

1. Check crack initiation/propagation.
   1.1 Compute non-local effective plastic strain in candidate elements.
   1.2 Compute damage variable if continuous damage model is used.
   1.3 If damage variable exceeds critical value, or effective plastic strain reaches criterion, active XFEM.
      1.3.1   For crack initiation, crack direction determined by first principal strain; for crack propagation, crack direction determined by damage/plastic strain center. Calculate crack line in the element in initial configuration.
      1.3.2   Add phantom nodes; replace the original shell element with two overlapping phantom elements which are comprised of real nodes and phantom nodes but have same element formulation as the replaced element.
      1.3.3   Calculate lumped mass for added phantom nodes and update lumped mass for the real nodes.

1.3.4   Constrain the phantom nodes on the crack tip edge.
2.   Update kinetical variables on real nodes and phantom nodes if any.
3.   Advance one time-step.
     3.1 Set nodal forces to zero.
     3.2 Apply external load, including contact force.
4.   Loop through regular finite elements and phantom elements.
     4.1 Calculate strain rate at Gauss points. Update strain components.
     4.2 Update stress components using continuous damage constitutive law.
     4.3 Calculate nodal forces at real nodes for all elements, and phantom nodes if it's a phantom element.
     4.4 If in a regular element the damage variable/effective plastic strain at any Gauss point exceeds the critical value, mark this element as an XFEM candidate.
5.   Go to 1.

2.2 Keyword for XFEM shells

XFEM shells can be activated using keyword *SECTION_SHELL. The keyword format is as follows

*SECTION_SHELL_{XFEM}

Card 1	1	2	3	4	5	6	7	8
Variable	SECID	ELFORM	SHRF	NIP	PROPT	QR/IRID	ICOMP	SETYP
Type	I	I	F	I	F	F	I	I

Card 3	1	2	3	4	5	6	7	8
Variable	MCID	BASELM	DOMINT	FAILCR	PROPCR	FS	LS/FS1	NC/LC
Type	I	I	I	I	I	F	F	F

ELFORM = 52 for 2D plain strain
        = 54 for shell
MCID: Material ID for cohesive law
BASELM =   2 for base shell element type 2 (default for shell)   = 13 for 2D plain strain (default for 2D)
        = 16 for base shell element type 16
DOMINT: Option for domain integration for XFEM
        = 0 phantom element integration (default)
        = 1 subdomain integration (not available in shell XFEM)
FAILCR: Failure criterion
        = 1 maximum tensile strength (value given in cohesive law)
        = -1 critical effective plastic strain
        = -2 crack length dependent EPS
        = -3 continuum damage model
PROPCR: Option for crack propagation direction
        = 0 first principal total strain direction
        = 2 center of effective plastic strain
        = 3 damage center
FS: Failure strain/Failure critical value
LS: Length scale for strain regularization, >0 actives strain regularization, available for FAILCR=-1
NC: Number of cracks allowed. NC<0 (or NC=-99) activates element erosion for failed XFEM elements.
When FAILCR=-2, a crack-length dependent critical effective plastic strain is defined as

$$\varepsilon_{crit} = \varepsilon_0 - \min(1.0, \ l / l_c) * (\varepsilon_0 - \varepsilon_1)$$
(1)

where ε_0 is initial failure plastic strain FS, ε_1 is final failure plastic strain FS1, l_c is crack length LC at final plastic strain and l is crack length.

3. Nonlocal Processing for XFEM Shell

With continuum damage models or standard plastic constitutive models, the finite element simulations using local failure criterion are susceptable to the mesh sensitivity problem. To avoid the pathological localization of deformation and damage growth in XFEM shell computation, the integral-type of nonlocal modeling [4] is considered in this paper.

3.1 Nonlocal strain averaging in shells

In the integral-type of nonlocal model, the growth of variable in a material point X is no longer governed by the local property at the point, but by an averaged or nonlocal property. In a classical plasticity-induced damage model, the damage variable d generally is a function of the effective plastic strain $\varepsilon^{ep}(X)$. Therefore, a continuous form of the nonlocal effective plastic strain $\tilde{\varepsilon}^{ep}(X)$ can be defined by

$$\tilde{\varepsilon}^{ep}(X) = \frac{1}{\int_{\Omega_X^0} \psi^{R_{non}}(Y;X)d\Omega} \int_{\Omega_X^0} \psi^{R_{non}}(Y;X)\varepsilon^{ep}(Y)d\Omega, \ \forall X \in \Omega^0 \tag{2}$$

where Y denotes the position of the infinitesimal volume $d\Omega$, and $\psi^{R_{non}}(Y;X)$ is a weight function that determines the influence of the local effective plastic strain $\varepsilon^{ep}(Y)$ in this infinitesimal volume on $\tilde{\varepsilon}^{ep}(X)$. In this study, the cubic spline function is used as the weight function. The radius size R_{non} of $\psi^{R_{non}}(Y;X)$ is a material length parameter which can be related to the scale of the microstructure [26] in a damage-induced strain localization problem. Ω_X^0 denotes a nonlocal processing zone of the evaluated material point X that is defined on the initial configuration Ω^0. The general application of Eq. (2) to the shell structures requires some modifications which are described as follows.

Considering a typical curved shell structure which is discretized by a set of quadrilateral elements as shown in Figure 1, we define an image of a material point X on the shell midsurface to be $\overline{X}$ on $\overline{\Omega}^0$. The two-dimensional domain $\overline{\Omega}^0$ is considered to contain a collection of shell elements projected from the three-dimensional space onto a two-dimensional domain based on the element associated with the evaluated material point X.
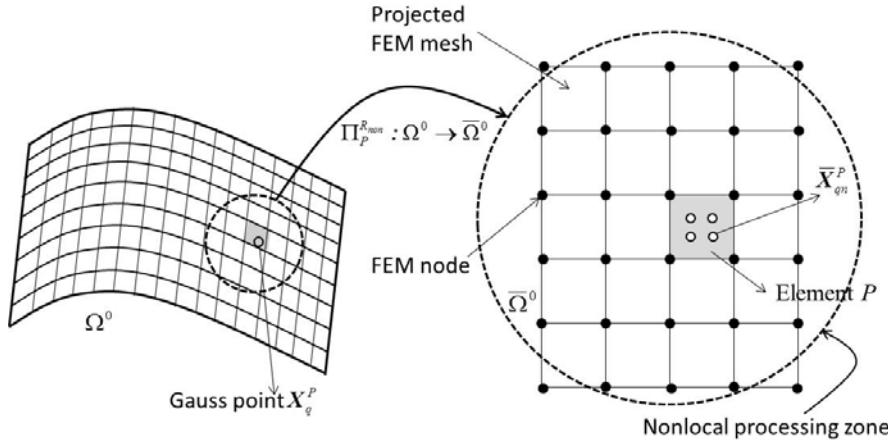
Figure 1. A projection of the shell midsurface in three-dimensional space to two-dimensional domain $\overline{\Omega}^0$ within the radius size R_{non} of the nonlocal processing zone

In other words, we first choose the element P in Ω^0 to be the coordinate plane to project the shell midsurface onto as well as to define the unit vectors for projection. Next, we determine the region of the projection by gathering the neighboring elements of element P that are within the nonlocal processing zone. Let X_{qm}^P denote a Guass point of element P where $q=1\sim4$ are four in-plane integration points and $m=1\sim(2*n+1)$ indicate the thickness integration points. We also let X_{qn}^P be a Guass point of element P on the shell midsurface. The projection is defined by

$$\Pi_P^{R_{non}} : \Omega^0 \to \overline{\Omega}^0 , \overline{X}_{qn}^J = \Pi_P^{R_{non}} \left(X_{qn}^J \right) \quad \forall X_{qn}^J \in \text{supp}\left(\psi^{R_{non}} \left(X_{qn}^P , X_{qn}^J \right) \right) \subset \Omega^0 \tag{3}$$

Apparently, we have $\overline{X}_{q1}^J = \overline{X}_{q2}^J = \ldots = \overline{X}_{qn}^J = \overline{X}_{q(2n)}^J = \overline{X}_{q(2n+1)}^J$ due to the projection made on the shell midsurface.

Since the quadrilateral shell element is completely cut by a crack, the crack front position can always be determined and defined on $\overline{\Omega}^0$. Giving a line of discontinuity and its crack front as shown in Figure 2, the position of the Gauss point $\overline{X}_{qm}^P$ in next fractured element and the corresponding nonlocal effective plastic strains can also be computed. Using Eq. (2), the nonlocal effective plastic strain $\tilde{\varepsilon}^{ep} \left(\overline{X}_{qm}^P \right)$ at the Gauss point $\overline{X}_{qm}^P$ in a non-cracked shell element P is computed by

$$\tilde{\varepsilon}^{ep} \left(\overline{X}_{qm}^P \right) = \frac{1}{\sum\limits_{I=1}^{NP} \overline{\psi}^{\overline{R}_{non}} \left(\Pi_P^{R_{non}} \left(X_{qn}^I \right), \overline{X}_{qn}^P \right)} \sum\limits_{I=1}^{NP} \overline{\psi}^{\overline{R}_{non}} \left(\Pi_P^{R_{non}} \left(X_{qn}^I \right), \overline{X}_{qn}^P \right) \varepsilon^{ep} \left(\Pi_P^{R_{non}} \left(X_{qm}^I \right) \right) \tag{4}$$

where NP is the total number of Gauss points within the radius size for nonlocal strain averaging. In this study, the $\overline{\psi}^{\overline{R}_{non}}$ is considered a projection of $\psi^{R_{non}}$ onto $\overline{\Omega}^0$ where the radius size $\overline{R}_{non}$ of $\overline{\psi}^{\overline{R}_{non}}$ is determined from a numerical calibration based on a simple tension test which will be described in the second numerical example in Section 4.
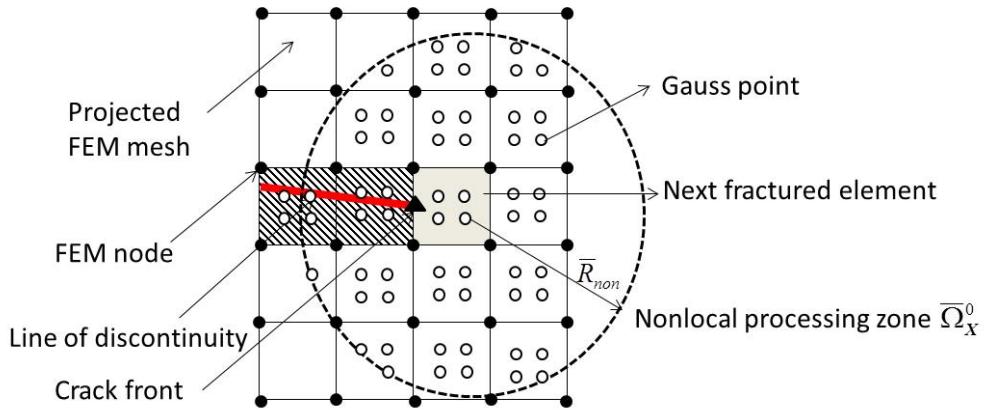
Figure 2. An illustration of nonlocal strain smoothing algorithm in this study

3.2 Crack propagation direction in shells

As soon as the damage variable at any one of the Gauss points in the element ahead of the current crack front reaches the critical value, the crack starts to propagate. Subsequently, the extension of the discontinuity will need to be made which requires the determination of crack propagation direction. Several approaches have been proposed for the determination of crack propagation direction in ductile fracture analysis [27, 28]. In this study we follow the approach of [27] and assume that no crack branching occurs in ductile fracture process. A damage center $\overline{X}^C$ in front of the crack is determined in the reference configuration by

$$\bar{X}^C = \sum_{J \in G_K} \frac{\Pi_P^{R_{non}}\left(X_{qm}^J\right)\exp\left(d\left(\Pi_P^{R_{non}}\left(X_{qm}^J\right)\right)\right)}{\sum_{J \in G_K}\exp\left(d\left(\Pi_P^{R_{non}}\left(X_{qm}^J\right)\right)\right)}, \ \forall \bar{X}^C \in \bar{\Omega}_0 \tag{5}$$

where the G_k is a node set that collects all the candidates of Gauss points including those through the thickness within the first half of the domain of influence in the nonlocal processing zone as shown in Fig 3. In other words, the damage value is weighted with the exponential function in Eq. (5) for the determination of the damage center $\bar{X}^C$.
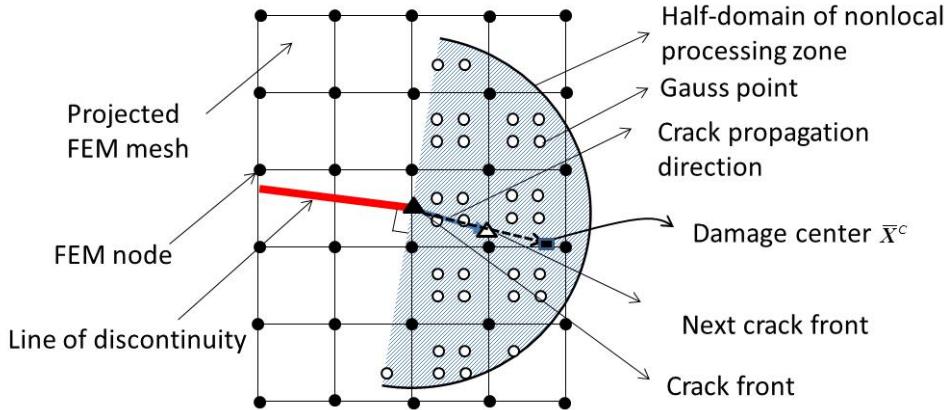
Figure 3. The determination of crack propagation direction in this study

While the direction of the discontinuity line is determined in the crack propagation step, the location of the crack front due to the assumptions of the through-the-thickness and element-wise discontinuous velocity and angular velocity fields remains to be predicted. In this paper, the location of the new crack front is determined by the intersection between the extension of the discontinuity line and the edge of the finite element ahead of the current crack front as shown in Figure 3. Once the new crack front is determined, the through-the-thickness and element-wise discontinuous velocity/angular velocity fields are added in the element formulation using the XFEM phantom-node approach to respect the stress-free condition when the material is fully degraded. This implies that the damage center X^C in the reference configuration Ω^0 and its crack propagation direction are also determined. The main reason of obtaining the crack propagation direction in the reference configuration is the same as that for most discontinuous approaches in fracture analysis [3,27,28]. That is to avoid the reformulation of the weak form problem due to the moving discontinuities.

4. Numerical examples

In this section, three benchmark examples are analyzed to study the performance of present method in the shell fracture analysis. It is assumed that ductile failure occurs mainly due to plastic straining so critical effective plastic strain criterion is used for crack initiation and propagation. Unless otherwise specified, dimensionless unit system is adopted in this paper.

4.1 Pulling test of 2D plate with a hole

Single crack propagation is studied in a 2D plate with a hole model using quasi-static nonlinear analysis. The model is shown in Figure 4. The strain-hardening elastic-plastic material properties are: Young's modulus E=100, Poisson's ratio v=0.3, and an isotropic hardening rule $\sigma_y\left(\bar{e}^p\right)=\sigma_y^0\left(1+\alpha\bar{e}^p\right)^\beta$ with coefficients $\sigma_y^0=0.75$, $\alpha=12.5$ and $\beta=0.05$. $\bar{e}^p$ denotes the effective plastic strain and $\sigma_y\left(\bar{e}^p\right)$ is the flow stress which is a scalar and increases monotonically with the effective plastic strain. Figure 5 shows three meshes with 773, 3062 and 6567 elements (mixed quadrilateral and triangular elements).

A damage law is taken [6, 28, 29] in the following form.

$$d = g(\kappa) \tag{6}$$

$$g(\kappa)=\begin{cases} \dfrac{\kappa_c(\kappa-\kappa_i)}{\kappa(\kappa_c-\kappa_i)} & if \quad \kappa_i \leq \kappa \leq \kappa_c \\ 0.99 & if \quad \kappa > \kappa_c \end{cases} \tag{7}$$

where κ_i and κ_c denotes the initial and critical values of effective plastic strain κ, respectively. The damage parameters are κ_i =0.09 and κ_c =0.1 while the radius of nonlocal processing zone R_{non} is fixed at 1.5 for all three discretizations.
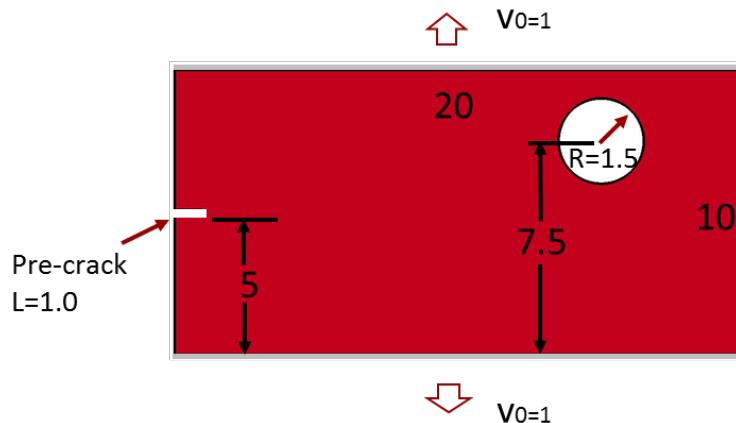
Figure 4. 2D plate with hole

(a) 773 elements   (b) 3062 elements   (c) 6567 elements
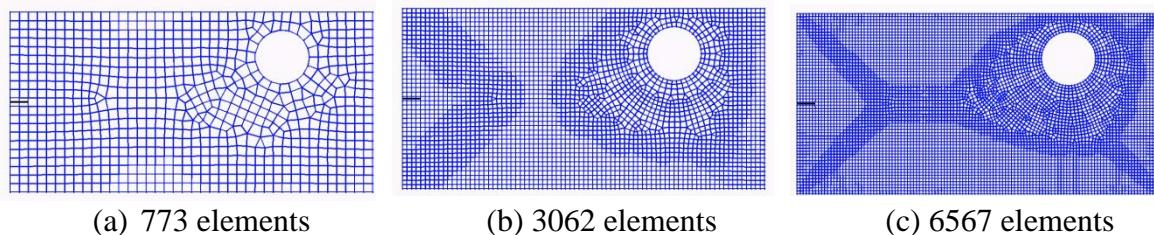
Figure 5. Three models with mesh refinement

(a) 773 elements   (b) 3062 elements

(c) 6567 elements
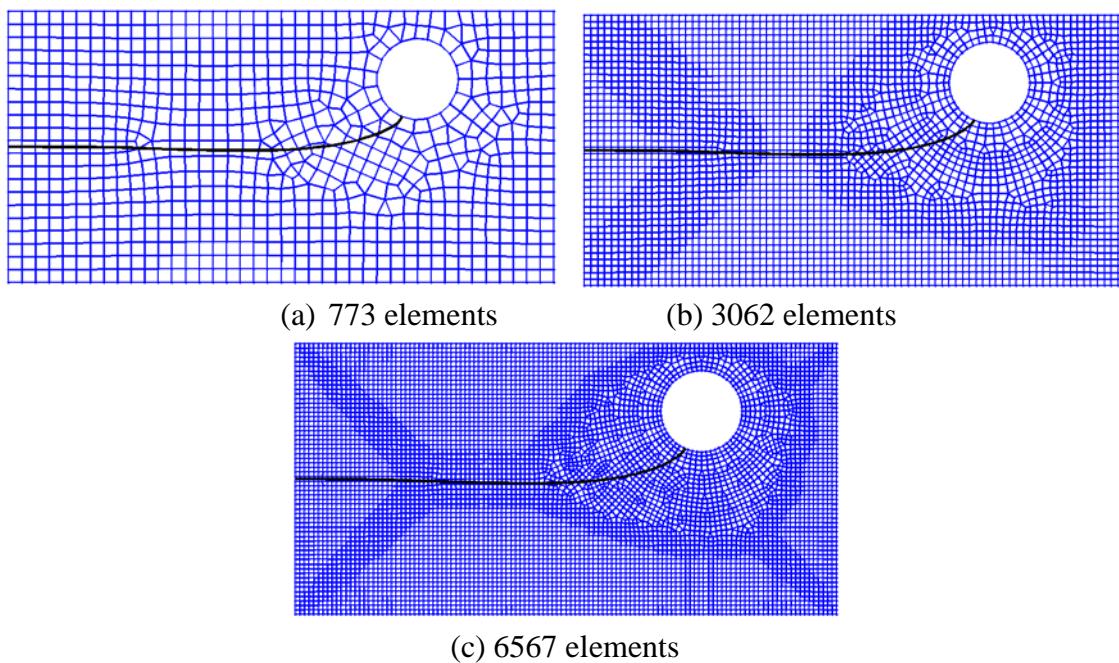
Figure 6. Final crack path results of three discretizations in the undeformed configuration

Figure 6 shows the final crack path results, which are very consistent across different mesh refinements. Figures 7 and 8 show the effective plastic strain and maximum principal stress results at three different crack propagation stages using the finest model.
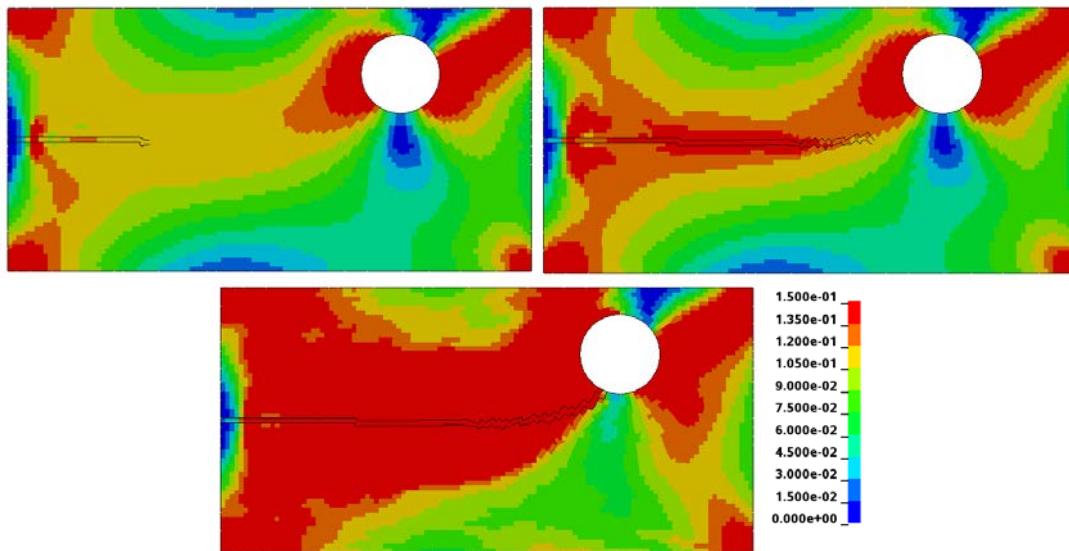
Figure 7. Effective plastic strain plots at three different crack propagation stages using the finest model (6567 elements)
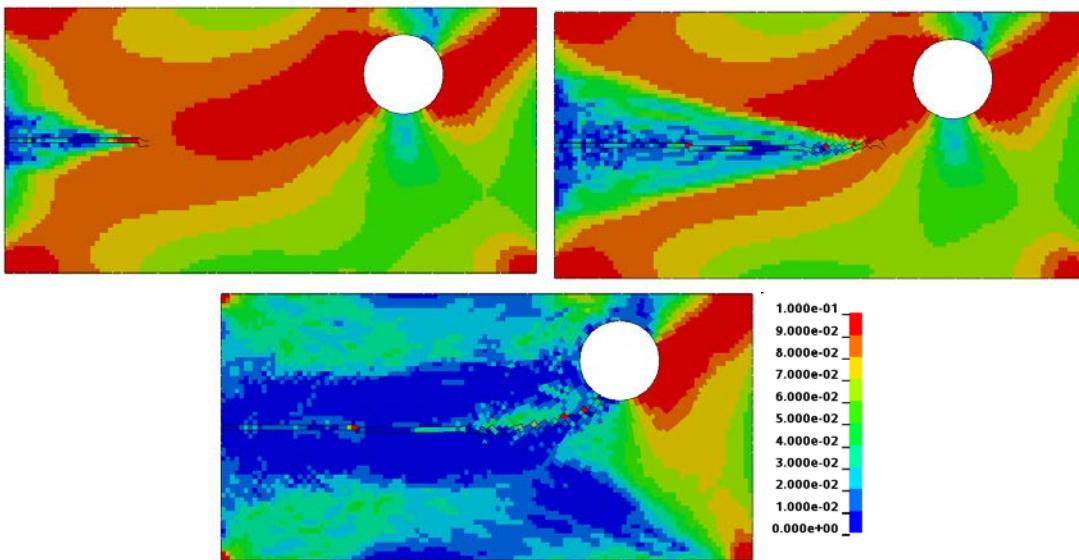
Figure 8. Maximum principal stress plots at three different crack propagation stages using the finest model (6567 elements)

Figure 9 shows the convergence study of boundary reaction force in y direction using three different refinements. Without nonlocal processing, the force response indicates quite different crack initiation time and crack speed for different meshes, while the results become consistent when using nonlocal processing.

(a) without nonlocal processing   (b) with nonlocal processing
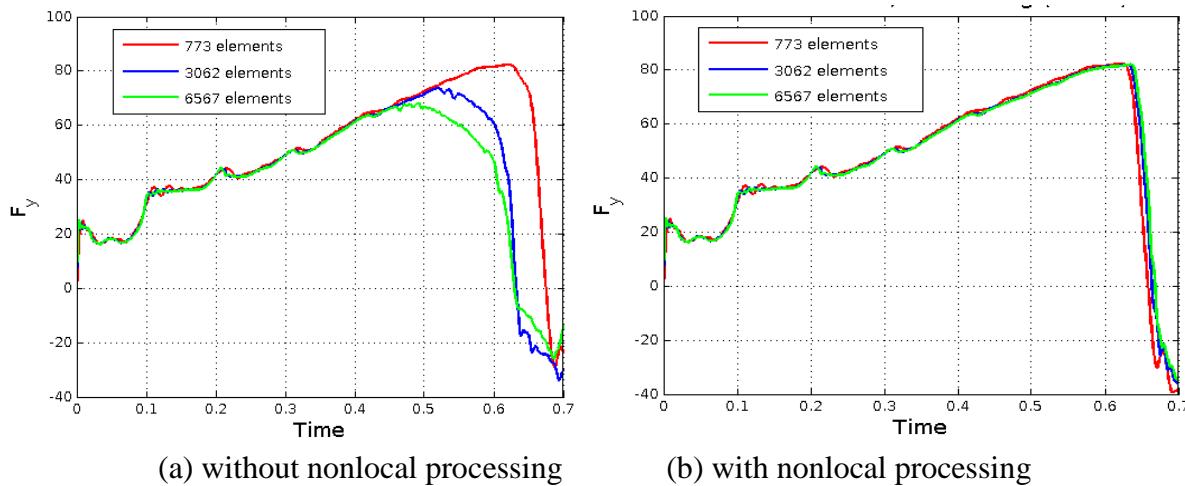
Figure 9. Convergence study of boundary reaction force results

4.2 Double V-notched specimen under stretching

In the second benchmark, a specimen with double V-notches is under uniaxial tensile stretching. This benchmark is used not only to demonstrate the mesh sensitivity problem of the local constitutive model, but also to illustrate a numerical mean to obtain the regularization length scale required in the non-local model.
The geometry of the specimen is shown in Figure 10 and the unit of length is millimeter. The lower edge of the specimen is fixed and the upper edge is clamped and pulled upwards with a constant velocity V_y=10mm/s. The material of the specimen is hot stamped high strength steel with density 7.8×10^{-9} ton/mm³, Young's modulus 1.8×10^5 N/mm², Poison's ratio 0.3, initial yield stress 1110.8 N/mm² and a non-linear yield stress-plastic strain

curve given in Figure 11. The critical effective plastic strain is 0.05. Due to symmetry, only half of the specimen is modeled in this study.
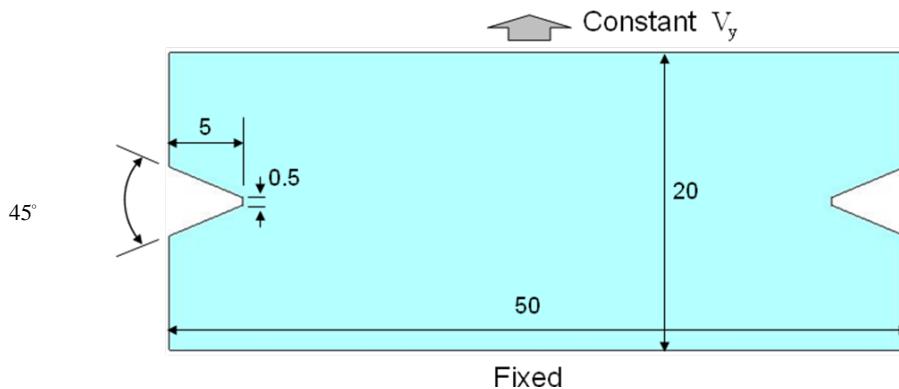
Figure 10. Double V-notched specimen under stretching
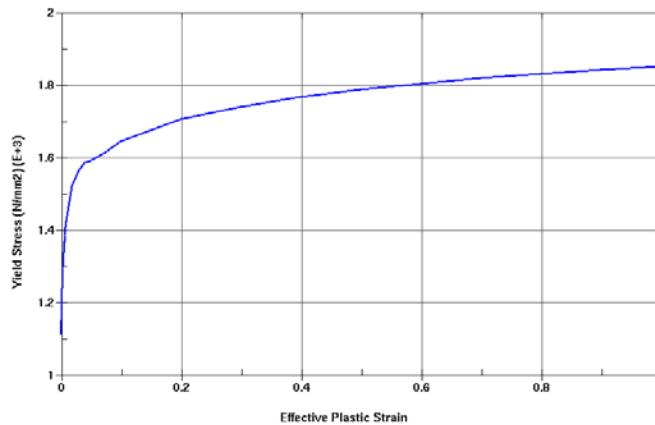
Figure 11. Non-linear yield stress-plastic strain curve

(a) 1840 elements   (b) 7360 elements   (c) 29440 elements   (d) 117760 elements
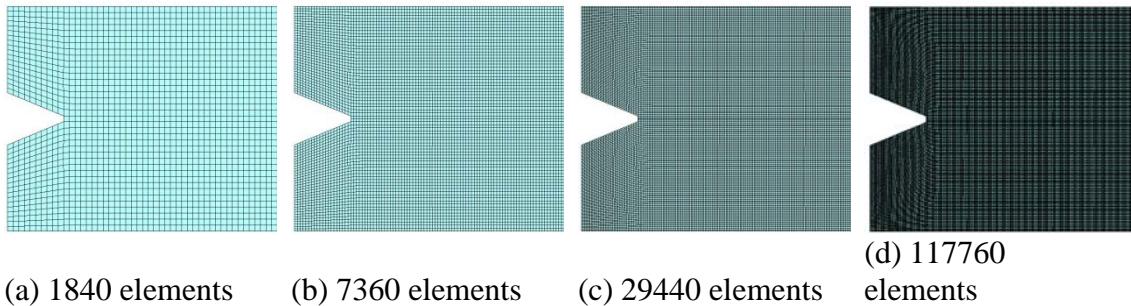
Figure 12. Four uniformly refined meshes

For the convergence study, a set of four uniformly refined meshes are used as shown in Figure 12. First, we simulate the problem with local constitutive model. The reaction forces on the moving boundary are plotted in Figure 13. From the results, we see that, with different mesh density, the reaction force history changes drastically with different crack initiation times and possesses quite different slope, indicating different crack propagation speed. This is the effect of mesh sensitivity and is caused by the strain localization existing in the continuous model. This mesh sensitivity problem can be remedied by the nonlocal processing.

Next, we conduct three numerical tests using different values of the regularization length scale, namely 1.0mm, 1.5mm and 2.0mm. The reaction forces obtained by the numerical tests are shown in Figure 14 (a)-(c). From the results, we can see that the effect of mesh sensitivity is minimized. The results from Mesh c and Mesh d are

almost identical, indicating the solution converges. We also notice that the reaction force at the crack initiation increases with the value of regularization length scale. Based on the results of our numerical tests, the relationship of the reaction force at the crack initiation to the regularization length scale can be simplified as a linear equation and expressed as following equation by linear regression:

$$F_c = 5.500\overline{R}_{non} + 39.08 \tag{8}$$
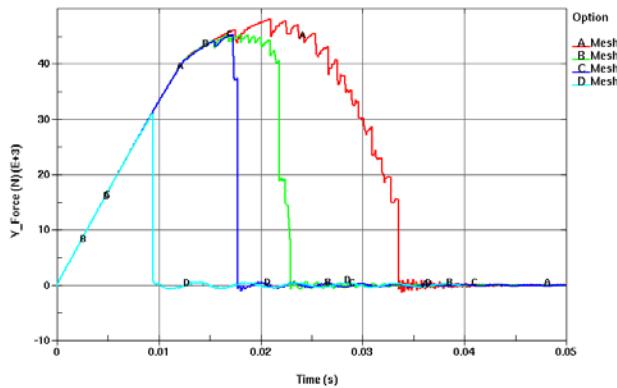
Figure 13. Reaction forces by different meshes without regularization
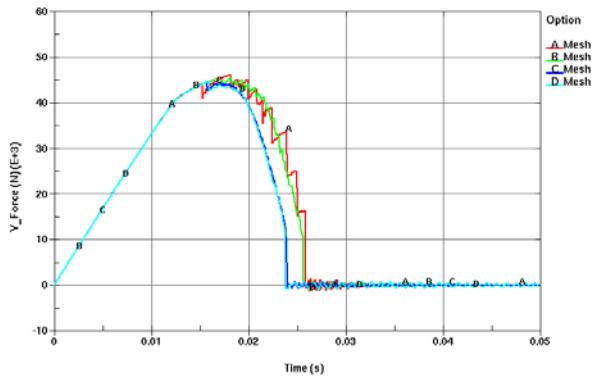
(a) $R_{non} = 1.0$mm
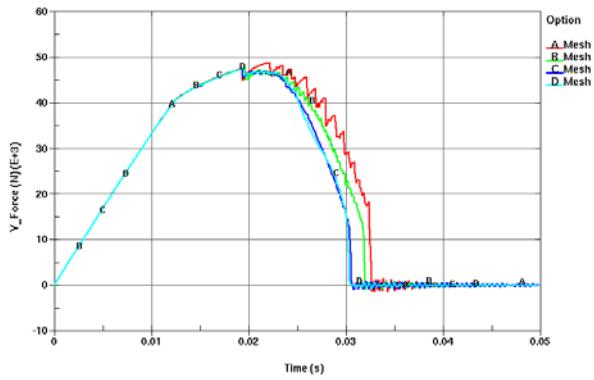
(b) $R_{non} = 1.5$mm
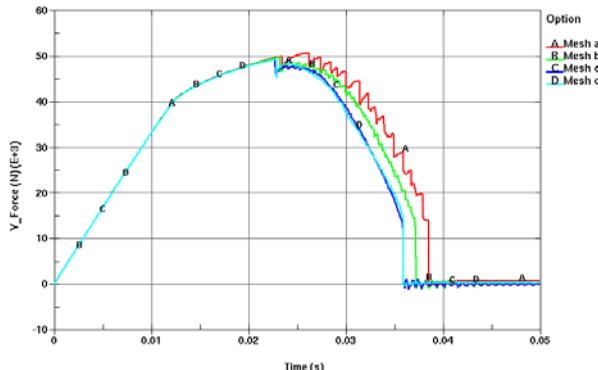
(c) R_{non} =2.0mm

Figure 14. Reaction forces by different regularization length scales

With the experimental results provided by Honda, the averaged total stroke force at the crack initiation is about 91.38kN and half of this force is 45.69kN, as shown in Figure 15. From the regression equation Eq. (8), we can calculate that the regularization length scale R_{non} of the hot stamped steel is 1.2mm, which will be applied to the three-point bending test in the next example.
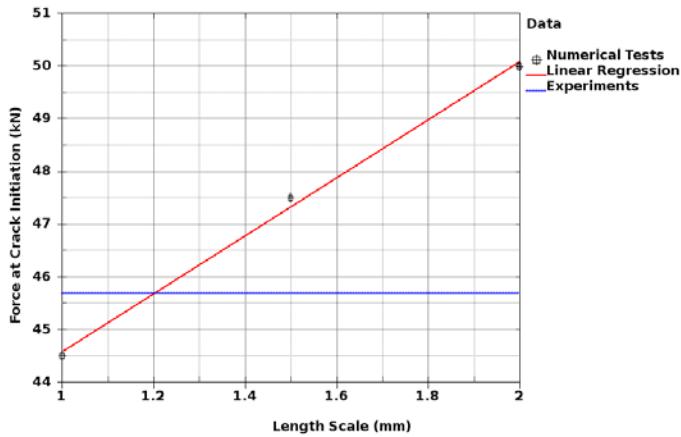
Figure 15. Reaction forces at crack initiation

4.3 Three-point bending of U-shaped beam with holes

In this numerical example, the fracture of a U-shaped steel beam with holes under three-point bending is studied. The model set up of the U-shaped beam is illustrated in Figure 16. The U-shaped beam of length of 600mm, which is connected to a backing plate with nuts and bolts, sits over a pair of metal rods of radius of 15mm that are located 500mm apart, and is pushed down by another metal rod of radius of 150mm in the middle of the beam with a constant velocity of 500mm/s. The cross section of the beam and the backing plate is shown in Figure 17 (a), where the thickness of both the U-shaped beam and the back plate is 1.6mm. The beam has an open notch in the center of the bottom surface with a width of 10mm and a depth of 5mm and half circular cuts on the side surfaces. It also has one pair of holes on the side surfaces of a diameter of 15mm located 31mm above the bottom surface and 15mm sideways off the middle of the beam, as shown in Figure 17 (b). The material of the U-shaped beam is hot stamped high strength steel, same as the material used in the previous example. The backing plate is made of JAC980YL steel. The two supporting rods and the punch rod are modeled as rigid material since their deformations are small compared to that of the beam.
The U-shaped beam is modeled with two meshes of different mesh densities. The coarse mesh has 41174 elements and the fine mesh has 164612 elements. The regularization scale of 1.2mm which is numerically calibrated from the previous example is used in this numerical example.
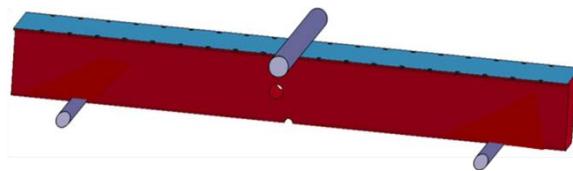
Figure 16. U-shaped steel beam under three-point bending
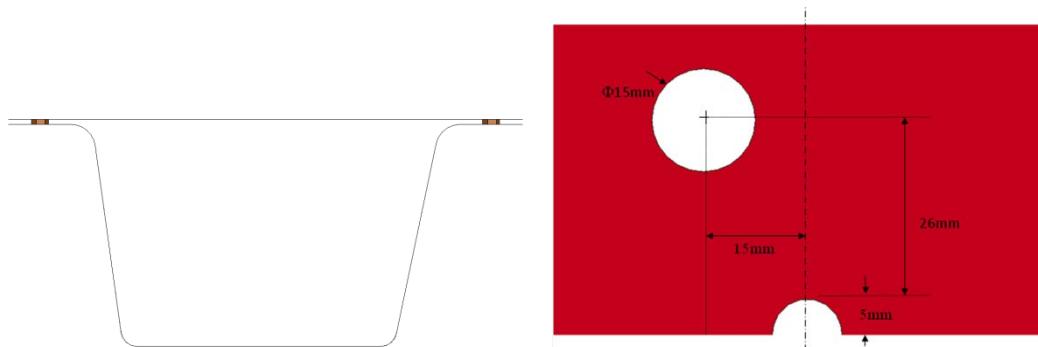
(a) Cross section of the beam   (b) Bottom notch and side holes

Figure 17. Cross section of the beam and openings on beam surfaces

Figure 18 shows the punch forces obtained with the two meshes to the relationship of the punch displacement. Compared to the experiment data, the fine model with the nonlocal processing constitutive law, correctly simulates the crack initiation time and peak punch force and the overall force profiles agree well with the experimental result.

Figure 19 shows the crack patterns at three different stages obtained with the fine model. There is no final crack pattern from the experiment corresponding to the numerical result, but we can see that there is material failure at the upper left side of the hole in the specimen, indicating there may be further crack propagation from there. Compared to the experimental results, we can see the numerical simulation captures the right crack pattern.
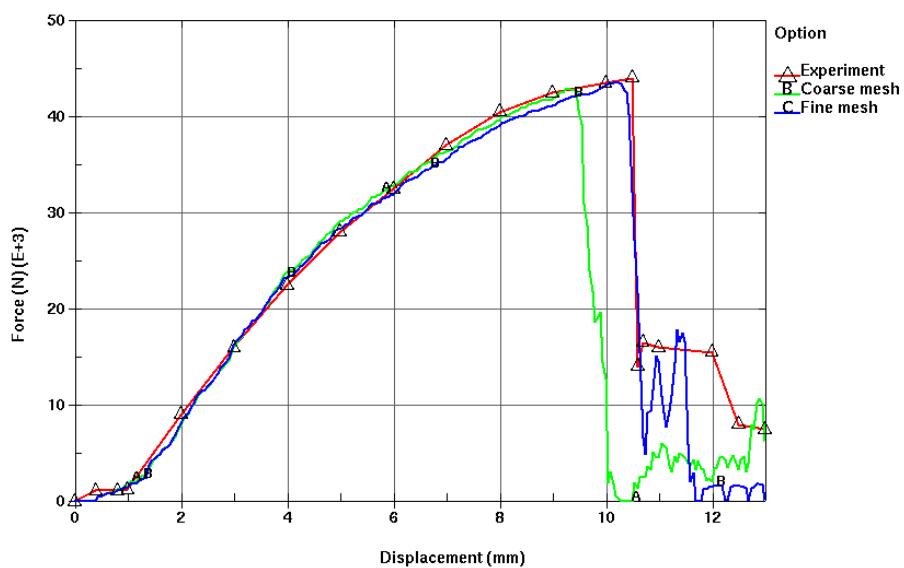
Figure 18 Punch forces vs punch displacement

(a) Initial crack   (b) Intermediate crack   (c) Final crack
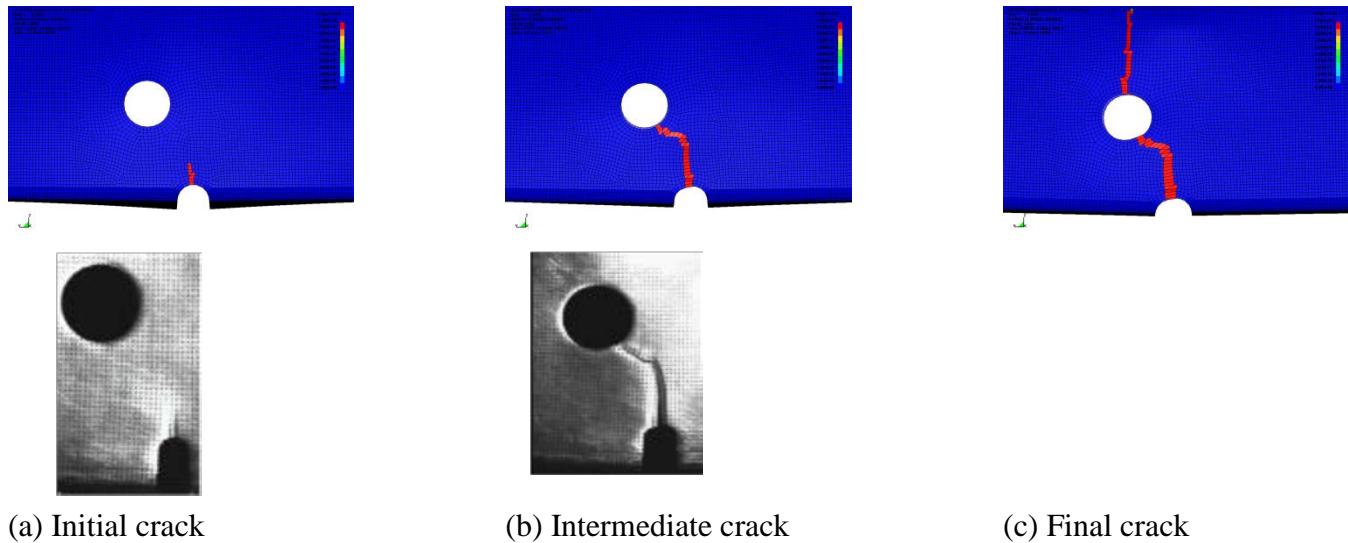
Figure 19. Crack patterns at different stages

5. Conclusions

The 4-node first-order shear-deformable shell element is simple and popular for modeling the mixed shell behavior in sheet metal forming and crashworthiness simulations for the past decades. In recent years, modeling the material failure in this type of shell has become critical for crashworthiness simulation in modern lightweight vehicle design. In this paper, a continuous-discontinuous approach based on the phantom-node XFEM method is applied to two widely used shell elements in LS-DYNA and is presented for the shell failure analysis. A nonlocal modelling procedure is introduced in this study to minimize the mesh sensitivity problem in ductile fracture analysis.

The numerical results in this study indicate that the present method is capable of simulating the discrete cracks in shell structures. Especially, the nonlocal algorithm developed in this study for XFEM shell formulation has been shown to effectively minimize the mesh sensitivity problem. A double V-notched test problem is utilized to calibrate the radius size of the nonlocal processing zone. The result is verified in the three-point bending test in which the present method successfully predicts the crack path with the right force response.

Acknowledgements

References

[1] Tai HW (1990) Plastic damage and ductile fracture in mild steels. Engng Fract Mech 36:583-580

[2] Chaboche JL (1988) Continuum damage mechanics. Part I: General Concepts, J Appl Mech 55:59-64

[3] Lemaitre J, Chaboche JL (1990) Mechanics of Solid Materials. Cambridge University Press, Cambridge

[4] Bažant ZP, Belytschko T, Chang TP (1984) Continuum theory for strain soften. J Engrg Mech 110:1666-1692

[5] de Borst R, Muhlhaus HB (1992) Gradient-dependent plasticity: formulation and algorithm aspects. Int J Numer Methods Engrg 35:521-539

[6] Chen JS, Wu CT, Belytschko T (2000) Regularization of material instabilities by meshfree approximations with intrinsic length scales. Int J Numer Methods Engrg 47:1303-1322

[7] Doan DH, Bui TQ, Duc ND, Fushinobu K (2016) Hybrid phase field simulation of dynamic crack propagation in functionally graded glass-filled epoxy. Compos Part B: Eng 99:266-276

[8] Seabra MRR, Cesar de Sa JMA, Andrade FXC, Pires FFMA (2011) Continuous-discontinuous formulation for ductile fracture. Int J Mater Form 4:271-281

[9] Mediavilla J, Peerlings RHJ, Geers MGD (2006) A robust and consistent remeshing-transfer operator for ductile fracture simulations. Comput Structures 84:604-623

[10] Mazars J, Pijaudier-Cabot G (1996) From damage to fracture mechanics and conversely: a combined approach. Int J Solid Struct 33:3327-3342

[11] Oliver J, Huespe AE, Pulido MDG, Chaves E (2002) From continuum mechanics to fracture mechanics: the strong discontinuity approach. Engrg Fract Mech 69:113-136

[12] Cazes F, Coret M, Combescure A, Gravouil A (2009) A thermodynamics method for the construction of a cohesive law from a nonlocal damage model. Int J Solids Structures 46: 1476-1490

[13] Oliver J (1996) Modeling strong discontinuities in solid mechanics via strain softening constitutive equations, Part I: Fundamentals. Int J Numer Methods Eng 39:3575-3600

[14] Moës N, Dolbow J, Belytschko T (1999) A finite element method for crack growth without remeshing. Int J Numer Methods Engrg 46:131-150

[15] Armero F, Linder C (2009) Numerical simulation of dynamics fracture using finite elements with embedded discontinuities. Int J Fract 160:119-141

[16] Hansbo A, Hansbo P (2004) A finite element method for the simulation of strong and weak discontinuities in solid mechanics. Comput Methods Appl Mech Engrg 193:3523-3540

[17] Song JH, Areias PMA, Belytschko T (2006) A method for dynamic crack and shear band propagation with phantom nodes. Int J Numer Methods Engrg 67:868-893

[18] Liu P, Bui TQ, Zhu D, Yu TT, Wang JW, Yin SH, Hirose S (2015) Buckling failure analysis of cracked functionally graded plates by a stabilized discrete shear gap extended 3-node triangular plate element. Compos Part B: Eng 77:179-193

[19] Yu TT, Bui TQ, Liu P, Hirose S (2015) A stabilized discrete shear gap extended finite element for the analysis of cracked Reissner–Mindlin plate vibration problems involving distorted meshes. Int J Mech Mater Des 12:85-107.

[20] Zeng Q, Liu Z, Xu D, Wang H, Zhuang Z (2016) Modeling arbitrary crack propagation in coupled shell/solid structures with XFEM. Int J Numer Methods Engrg 106:1018-1040

[21] Englemann BE, Whirley RG, Goudreau GL (1989) A simple shell element formulation for large-scale elastoplastic analysis. In Analytical and Computational Models of Shells. Noor AL, Belytschko T, Simo JC Eds., CED-Vol. 3, ASME, New York, New York.

[22] Hallquist JO (2006) LS-DYNA Theory Manual. Livermore Software Technology Corporation

[23] Belytschko T, Lin JI, Tsay CS (1984) Explicit algorithms for the nonlinear dynamics of shells. Comput Methods Appl Mech Engrg 42:225-251

[24] Dvorkin EN, Bathe KJ (1984) A continuum mechanics based four-node shell element for general non-linear analysis. Eng Comput 1:77–88

[25] Simo JC, Hughes JC (1986) On the variational formulation of assumed strain methods. J Appl Mech 53:1685-1695

[26] Bažant ZP, Planas J (1998) Fracture and Size Effect in Concrete and Other Quasibrittle Materials. CRC Press, Florida

[27] Broumand P, Khoei, AR (2013) The extended finite element method for large deformation ductile fracture problems with a non-local damage-plasticity model. Engrg Fract Mech 112-113:97-125

[28] Wu CT, Ma N, Takada K, Okada H (2016) A meshfree continuous-discontinuous approach for the ductile fracture modeling in explicit dynamics analysis. Comput Mech 58:391-409

[29] Wu CT, Wu YC, Koishi M (2015) A strain-morphed nonlocal meshfree method for the regularized particle simulation of elastic-damage induced strain localization problems. Comput Mech 56:1039-1054

[30] CT Wu, N. Ma, Y. Guo, W. Hu, K. Takada, H. Okada, K. Saito (2017) A dynamic ductile failure analysis of shell structures using a nonlocal XFEM method. Advances in Engineering Software, submitted.